Available online at www.sciencedirect.com

jmr&t Journal of Materials Research and Technology

journal homepage: www.elsevier.com/locate/jmrt

Original Article

Laser cutting of silicon anode for lithium-ion batteries

Mulugeta Gebrekiros Berhe [a], *Hong Geun Oh* [b], *Seung-Keun Park* [b], *Dongkyoung Lee* [a,c,d,*]

[a] *Department of Future Convergence Engineering, Kongju National University, Cheonan, South Korea*
[b] *Department of Advanced Materials Engineering, Chung-Ang University, Anseong, South Korea*
[c] *Department of Mechanical and Automotive Engineering, Kongju National University, Cheonan, South Korea*
[d] *Center for Advanced Powder Materials and Parts of Powder (CAMP²), South Korea*

ARTICLE INFO

Article history:
Received 16 September 2021
Accepted 24 November 2021
Available online 10 December 2021

Keywords:
Laser cutting
Silicon anode
Copper
ANOVA
Regression analysis

ABSTRACT

Lithium-ion batteries (LIBs) are vital in the transportation sector due to their promising technology meeting the future hybrid and electric vehicles requirements. The limited capacities of anode and cathode materials are the obstacle in the current state of LIBs to obtain good performance. Silicon (Si) has the highest capacity compared to the currently used graphite anode. In this study, laser technology was employed to perform cutting of silicon anodes, which previously have not been studied. First, the optical properties of silicon anode are measured, and four types of cutting widths such as top, kerf, clearance, and burr as well as five types of physical cutting phenomena such as excessive fill cutting, proper full cutting, partial cutting, partial melting of the current collector and full ablation of active material were defined and measured. Minimum average cutting power, as well as cutting and energy efficiencies, are established for all parameter groups. The effects of process parameters on the measured cutting widths are studied by developing mathematical models using multivariate regression based on the response surface method (RSM). The process parameters contribution was also analyzed using the analysis of variance (ANOVA). For the formation of kerf width, clearance width, and burr width the cutting speed have the largest contribution with percentages of 53, 55, and 67 respectively. The laser power also has a 65% impact on the formation of the top width.

© 2021 The Author(s). Published by Elsevier B.V. This is an open access article under the CC BY-NC-ND license (http://creativecommons.org/licenses/by-nc-nd/4.0/).

1. Introduction

Lithium-ion batteries (LIBs), which are secondary rechargeable batteries are one of the most important energy storage technologies playing a significant role in the development of electronic devices, electric vehicles, house appliances, and energy storage as a result the demand for them is increasing rapidly [1–4]. The popularity of LIBs over other batteries such as Ni–Cd and Pb-acid batteries is due to their high energy and power density, low self-discharge, and energy to weight ratio

* Corresponding author.
E-mail address: ldkkinka@kongju.ac.kr (D. Lee).
https://doi.org/10.1016/j.jmrt.2021.11.135
2238-7854/© 2021 The Author(s). Published by Elsevier B.V. This is an open access article under the CC BY-NC-ND license (http://creativecommons.org/licenses/by-nc-nd/4.0/).

[5–7]. LIBs such as Li–Fe phosphate, Li–Ni/Mn/Co oxide, and Li–Co oxide are mostly used nowadays.

The main components of a LIB are the anode where the Cu foil is sandwiched between graphite layers, cathode where the Al foil is sandwiched between lithium metal oxide layers, separator, and electrolyte [3]. The anode and cathode components of the battery are that mainly determine the output voltage and specific capacity, which are an indication of the electrochemical performance of the LIB [8–10]. For better improvement of battery performance, anode electrodes have more room for improvement than cathode electrodes [11–13].

Currently, graphite is the primary and most widely used anode material in LIBs, it has a moderate theoretical gravimetric capacity of 372 mAh/g [4,14,15]. However, graphite anodes exhibit some complications that hinder their potential such as low capacity, high cost, problem operating at low temperature, and safety issues [16,17]. As a consequence, silicon (Si) was found to be one of the suitable alternative anode materials to replace graphite due to its higher gravimetric capacity and volumetric capacity as it can be seen in Table 1. In addition, Si has a moderate working potential (0.5 V) and is the second most abundant element in the earth crust as well as environment-friendly [7–9,16–21].

LIB performance is not only reliant on anode material but is also altered by the manufacturing process, in addition, battery cost is mainly impacted by material and manufacturing cost [10,22]. Electrode cutting is one of the battery performance decisive processes because defects produced as a result of poor cut quality may result in performance degradation [23,24]. Currently, conventional electrode cutting means such as punching, slitting, and mechanical blanking are widely used. However, these methods result in poor cut quality, downtimes for tool repair and change, and unstable process due to tool wear [22–25]. Those current methods used for electrode cutting contribute to the rise in battery cost. Therefore, it is mandatory to introduce an advanced manufacturing technology to overcome these kinds of challenges. Hence laser cutting is a contactless process and promising alternative to conventional methods mentioned above as it is precise, reliable and there is no tool wear [23–26].

Even though the application of laser cutting is rare in the industrial production of battery electrodes, some researchers have been published in this area. Lee et al. [5], Lee [23], Lee and Ahn [24], Lee et al. [27], Lee and Suk [28], Lee et al. [29] focused on developing numerical studies of a mathematical model to analyze the cutting characteristics of electrodes. The developed mathematical model was employed to investigate laser cutting of cathode [24,27,29], anode [23,27,28] and current collectors [5]. Luetke et al. [30] used continuous and pulsed lasers to define the minimum cutting speed and appropriate laser power for cutting anode and cathode, which is comparable with mechanical punching with better process efficiency and quality. Lutey et al. [31] applied five different laser sources; 2 infrared (IR) (1064 nm) pulsed lasers, 1 continuous wave laser, and 2 green (532 nm) lasers with different power and speed parameter ranges to cut $LiFePO_4$ and analyzed the ablation depth of 3D profiled specimen using numerical functions. Lutey et al. [31] also additionally performed a parameter study using a nanosecond pulsed laser to cut $LiNiMnCoO_2$ (LNMC) cathode. Pulse duration, repetition rate, and laser fluence were varied to assess the cut quality and cutting characteristics. Dimir et al. [25] used green and IR nanosecond pulsed fiber lasers to study remote cutting of anode and cathode. The pulse duration was varied in this study, and they investigated the maximum cutting speed, which results in good quality and productivity. From an electrode material point of view, Si anode was used in developing 3D architecture and investigate the electrochemical properties [32].

After an extensive literature survey, it was observed that no work has been presented yet on the laser cutting of Si anode. Therefore, this study presents a new insight into laser cutting of Si anode for the first time. The effects of laser parameters and multi-physical phenomena are investigated by analyzing the top, kerf, clearance, and burr widths in addition to cutting efficiency. ANOVA and multiple regression analysis were also used to predict and investigate the effect of parameters in the laser–material interaction. The paper is organized as follows. First, materials, experiments, and measurements are explained. Second, the qualitative and quantitative analysis of laser cutting results is described. Next, the statistical methods for this study are explained. At last, the concluding remarks are mentioned according to the results obtained.

Table 1 – Capacities of Si and graphite anodes.

Material	Volumetric capacity (mAh/cm^3)	Gravimetric capacity (mAh/g)
Graphite	837	372
Si	9786	4200

2. Materials, experiments, and measurements

2.1. Materials

A slurry was prepared by mixing Si powder (crystalline, 100 nm, 99%, Alfa Aesar), Super P, and polyvinylidene fluoride (PVDF) binder, which the mixture later dissolved in 1-methyl-2-pyrrolidone (NMP, 99.5%). Si powder, Super P, and PVDF binder were mixed by weight ratio of 8:1:1 respectively. The slurry was coated on the one side of Cu foil with 20 μm thickness, followed by drying under vacuum at 40 °C for 40 min. After coating, the Si electrode was pressed by a roll press to set the total thickness of the electrode to 40 μm.

2.2. Experiments

A Ytterbium nanosecond pulsed fiber laser (YLPM, IPG photonics, Southbridge, Massachusetts USA) with an emission wavelength of 1070 nm feature was used as a laser source for this experiment. It could generate up to 300 W average laser power and operate up to a repetition rate of 2000 kHz, pulse duration of 200 ns, and cutting speed of 5000 mm/s. The laser source had also a beam quality factor (M^2) of 1.5, a collimated beam diameter of 7.2 mm, and a spot diameter of 40 μm. In industrial electrode production, nanosecond laser sources

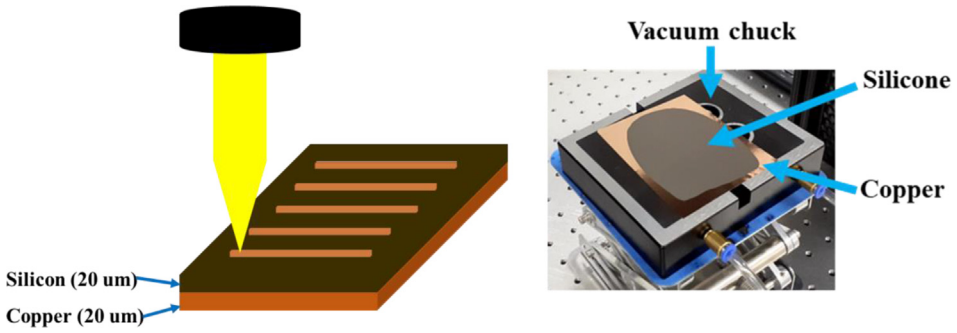


Fig. 1 – Experimental setup and sample.

with average laser power in the range of 100–300 W are commonly used for cutting due to low heat input, competitive cutting speed, and reasonable costs. A minimum cutting speed of 500 mm/s was set because below this value the process becomes unattractive for mass production of LIBs and cannot compete with conventional cutting methods. The tested Si anode material shown in Fig. 1, is comprised of 20 μm thick Cu current collector foil and 20 μm thick Si active material. The electrode material was prepared in 3.0 × 3.5 mm size and a vacuum chuck was used to keep the electrode flat and in tension. The working distance between the F-θ lens and the top surface of the sample was set to 180 mm. The laser parameters employed for this study are shown in Table 2.

2.3. *Measurements*

The schematic definitions of the measured top, kerf, clearance, and burr widths are shown in Fig. 2. Top width is the width of the active material of electrode removed by a laser, kerf width is the opened width of the fully separated electrode, the extended metal width from top width to the cutting edge is defined as clearance width and burr width is the width of the resolidified molten metal [24,28,33]. Scanning electron microscopy (SEM) was used to observe the electrode laser cutting physical phenomena. Three experiment repetition was held for every experiment to get reliable and efficient results.

3. Result and discussion

3.1. *Optical properties of materials: absorptivity, reflectivity, and transmittance*

The laser beam and material interaction phenomena are accompanied by absorption and scattering phenomena resulting in spatial distribution and attenuation of the beam energy [33,34] as shown in Fig. 3. When the laser beam is in interaction with material the part of a laser beam is absorbed and/or reflected or transmitted depending on the optical properties of the material. The absorbed heat energy as the result of the incident laser beam may heat, vaporize, melt, and ablate the material depending on the fluence, interaction time, and other laser input parameters. The spectrometry measured absorptivity, reflectivity, and transmissivity of Si are shown in Fig. 3. The absorptivity and reflectivity of Si anode at a wavelength of 1070 nm are 83.5% and 16.5% respectively. Similarly, Cu foil optical properties were measured in previous studies [28]. At a particular wavelength of 1070 nm, the absorptivity and reflectivity were found to be 1.92% and 98.08% respectively. However, both the Si and Cu foil were not laser beam transparent materials, so the transmittance was measured to be zero. Similarly, graphite anode exhibits absorptivity of 88.25% and reflectivity of 11.75% [28]. The relationship between these optical features of material can be expressed by Eq. (1)- [28].

$$\alpha_\lambda + \rho_\lambda + \tau_\lambda = 1 \quad (1)$$

where, α_λ, ρ_λ and τ_λ represents absorptivity, reflectivity, and transmittance, respectively.

3.2. *Laser cutting characteristics – qualitative analysis*

The quality of laser cut samples was observed using SEM to quantify the above-defined widths for cut quality evaluation. A full set of SEM pictures taken are presented in Figure 6, 7, 8 and 9 to see the change of cut quality easily. The pictures in these figures indicate all samples tested with different power and speed parameter variations. Five different types of cutting phenomena such as excessive full cut of the electrode, proper full cut of the electrode, partial cut of the electrode, partial melting of the current collector, and full ablation of active material were observed as shown in Fig. 4. These physicals phenomena occur because of the combination of heat

Table 2 – Laser parameters used for the experiment.

Laser parameters	Investigated range
Power	50–250 W (50 range)
Cutting speed	500–5000 mm/s (500 range)
Pulse repetition rate	500 kHz
Pulse duration	60 ns

Table 3 – Optimal laser parameters.

Width	Power (W)	Speed (mm/s)	Width (um)
Top	150	3957.83	98
Kerf	224.81	3281.06	17
Clearance	150	1359.43	37
Burr	235.99	2484.87	15

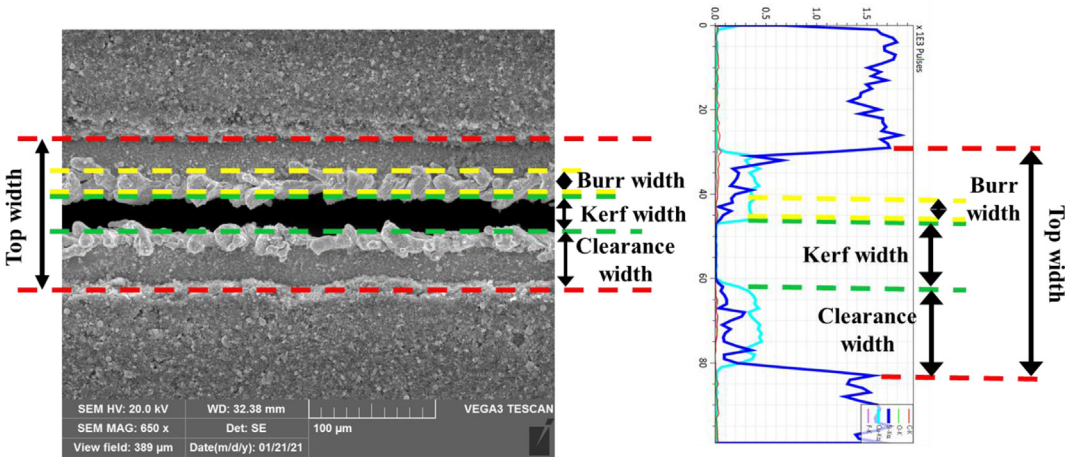


Fig. 2 – Schematic measurement definitions using sample SEM and energy dispersive spectroscopy results.

conduction, heat convection, melting, evaporation, and re-solidification.

The five different cutting phenomena described above can be shown according to their volume energy in Fig. 5. The volume energy as defined somewhere in [27,28] is given by Eq. (2). The cutting characteristics include excessive full cutting of electrode, proper full cutting of electrode, a partial cutting of electrode, partial melting of the current collector, and full ablation of active material. The volume energy [24] required increases in producing the phenomena of full ablation of active material, partial melting of the current collector, a partial cutting of electrode, proper full cutting of electrode, and excessive full cutting of electrode in respective order. The volume energy to produce these cutting phenomena ranges between 7.96×10^9 - 3.98×10^{11} J/m^3. The volume energy range of partial cutting of electrode, proper full cutting of electrode, and excessive full cutting of electrode were overlapped.

$$\text{Volume energy}\left(\frac{J}{m^3}\right) = \frac{\text{Power (W)}}{\text{Cutting speed}\left(\frac{mm}{s}\right) \times \text{Spot area}\,(mm^2)} \quad (2)$$

SEM images with laser power of 50 W are shown in Fig. 6. Three kinds of physical cutting phenomena such as:(i) excessive full cutting of electrode; (ii) partial melting of the current collector; and (iii) full ablation of active electrode material were observed. With laser cutting speed of 500 mm/s full cutting of electrode with narrow kerf width is observed. From laser cutting speed of 1000–4000 mm/s the dominant phenomena of partial melting of the current collector where the melted amount decreases with increasing speed can be seen from the closer inspection of SEM image. And when the maximum cutting speeds of 4500 and 5000 mm/s are employed full removal of active electrode material occurred with less damage on the current collector. All samples exhibit a visible top width, which decreases when laser cutting speed increases even though the degree of change is small. The other two, clearance and burr widths are observed in laser cutting speed of 500 mm/s only.

Figure 7 shows SEM images of the resulting electrodes following laser exposure at 100 W. Within this category excessive full cutting of electrodes are exhibited in cutting speeds of 500 and 1000 mm/s. Proper full cutting of electrode

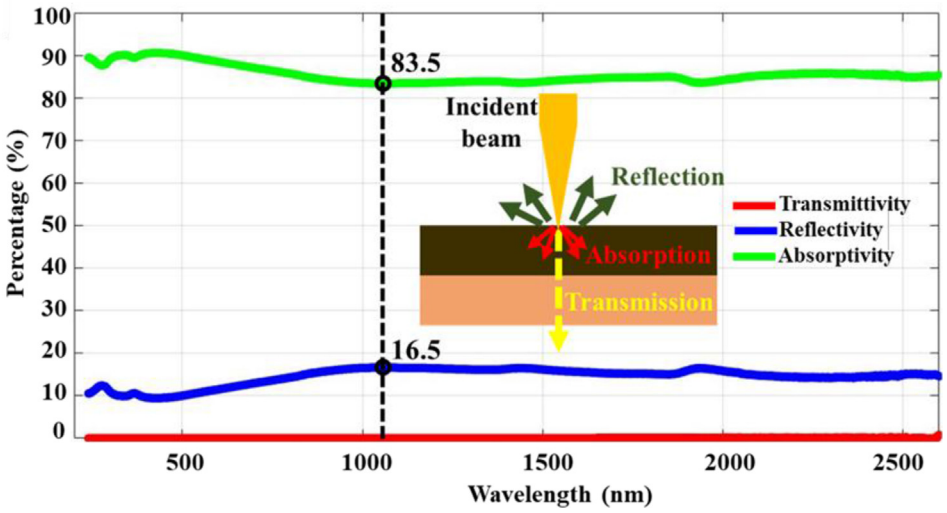


Fig. 3 – Absorptivity, reflectivity, and transmissivity measurements of Si anode.

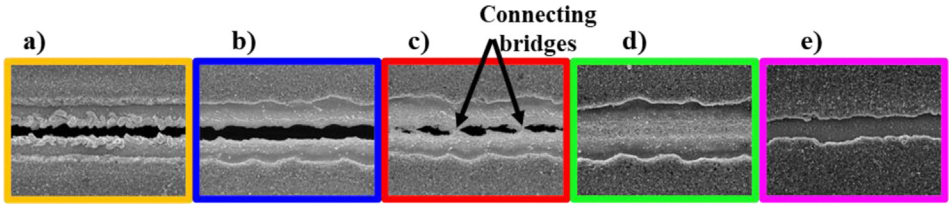


Fig. 4 – Different cutting phenomena: (a) Excessive full cutting (b) Proper full cutting (c) partial cutting (d) Partial melting of current collector (e) Full ablation of active material.

occurred on the next 1500 and 2000 mm/s employed cutting speeds. Partial melting of the current collector can be seen starting from 2500 to 5000 mm/s. The top width forms a wavey zigzag type shape starting from 2000 to 5000 mm/s and width decreases with increasing cutting speed. The formation of burr is also strongly noticed in 500 mm/s and decreases with the raising cutting speed for all fully cut electrodes. These burrs are formed when the melted copper current collector resolidify quickly. All fully cut electrodes also show visible clearance width. The clearance width is where the active electrode material is removed over larger width than the current collector.

The resulting SEM images obtained under laser powers of 150 and 200 W are shown in Figs. 8 and 9. For laser power of 150 W, excessive cutting of electrode was seen in cutting speeds of 500 and 1000 mm/s, proper cutting of electrode from 1500 to 2500 mm/s, a partial cutting of electrode at 3000 and 3500 mm/s, and partial melting of the current collector occurred in cutting speed range of 4000–5000 mm/s. For laser power of 200 W excessive cutting of electrode is observed in cutting speeds of 500 and 1000 mm/s, proper cutting from 1500 to 3000 mm/s, a partial cutting of electrode in 3500 and 4000 mm/s, and partial melting of the current collector is seen in cutting speed of 4500 and 5000 mm/s. Excessive burr is remarked in cutting speeds of 500 and 1000 mm/s. Similar to laser powers of 50 and 100 W wavey and zigzag-shaped top width with increasing cutting speed was also realized at laser powers of 150 and 200 W. In contrast, the prior laser powers employed the largest cutting widths are observed at these laser powers. The full-cut electrodes exhibit visible kerf, burr, and clearance widths. The clearance width is formed due to the ablation threshold difference between the active material and current collector or heat accumulation and conduction effects from the current collector leading to heating and removal of active material.

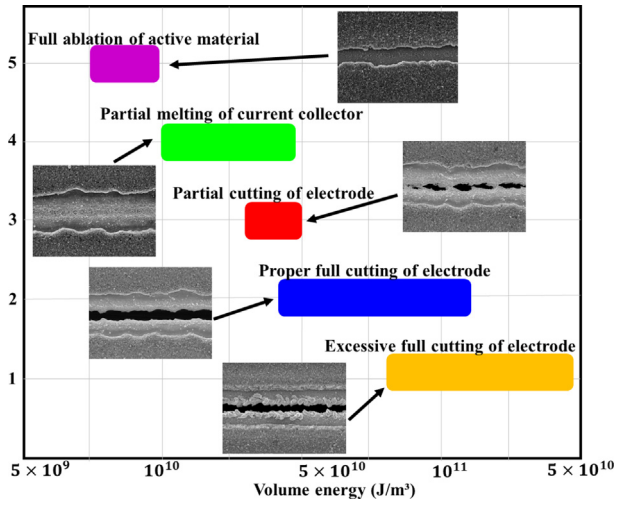


Fig. 5 – Cutting phenomena according to volume energy.

Figure 10 shows the SEM images with a laser power of 250 W and four types of cutting phenomena are observed. Excessive cutting occurred at cutting speeds of 500 and 1000 mm/s, proper cutting in the range of 1500–3500 mm/s, a partial cutting of electrode at 4000 and 4500 mm/s, and finally partial melting of the current collector at 5000 mm/s. The top width shows less degree of change and gets zigzag and wavey shape with increasing cutting speed. In all laser, powers employed the cut edge quality increase as the cutting speed increase. It is also observed that the burr at the cutting-edge decreases and the edge gets smoother as the cutting speed increases. The reason for this is decreasing pulse overlap in respective to laser material interaction time at a high cutting speed, which is not sufficient to produce molten in the cutting edge. At high cutting speeds, all widths are the result of the direct laser beam as heat conduction effects become less significant.

The minimum average cutting power and corresponding laser fluence for each cutting speed employed are presented in Fig. 11 for all parameter groups. Within the experimental group, the minimum cutting energy input was obtained at 500 mm/s, which is 7.91 J/cm^2. Maximum input energy of 39.78 J/cm^2 was required to produce full film penetration at a cutting speed of 3500 mm/s as the interaction time is less here compared to in smaller cutting speeds. Cutting speeds of 1000, 1500, and 2000 mm/s required the same minimum cutting power of 100 W. When the cutting speed increase, they require higher minimum average cutting power. The implication of these results is important from a productivity and economic point of view as proper selecting of parameters is one influencing factor.

3.3. *Laser cutting characteristics – quantitative analysis*

The top width in relation to cutting speed and volume energy for each employed laser power is shown in Fig. 12. The top width decreases with increasing cutting speed and vice versa top width increases with increasing volume energy. The excessive cut electrode top widths were measured in the range of 105–184 μm, for proper cut electrode it ranged

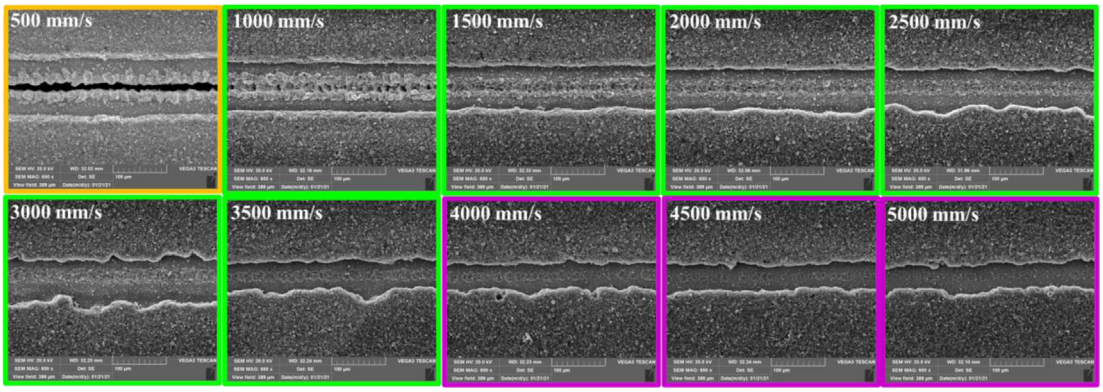


Fig. 6 – SEM image for the laser power of 50 W.

between 98 and 164 μm, for partial cut electrode measured to be from 102 to 124 μm, for a group where they exhibited it ranged from 62 to 116 μm and for electrode where full ablation of active material only occurred ranges from 43 to 51 μm. The minimum top width measurement ranges from 43 to 184 μm, which are all larger than the focused spot size. Therefore, the heat accumulation and conduction effects from the current collector led to heating and removal of active material. However, under high cutting speed and lower laser powers, the top width is mostly a result of direct laser exposure since the top widths are approximate to the beam spot size. The threshold volume energy to form the top width between the two counterpart active material surfaces is between 7.96×10^{9} - 3.98×10^{11} J/m^3.

Figure 13 shows the kerf width analyzed in terms of cutting speed and volume energy. The kerf width is not formed for laser powers of 50, 100, 150, 200, and 250 W. When the cutting speed is faster than 1000, 2500, 3000, 3500, and 4000 mm/s respectively in their order. As the cutting speed increases the kerf width gets narrower and when the input volume energy increases the kerf width gets broader as the heat conduction loss becomes more significant in addition to the direct laser exposure [35]. Relative to laser powers of 200 and 250 W, the kerf width falls fast in the laser powers of 50, 100, and 150 W consecutively and has a high degree of change. The maximum kerf width was measured to be 39 μm when using the laser powers of 200 and 250 W at a cutting speed of 500 mm/s. According to volume energy, volume energy in the range of 3.98 $\times 10^{10}$–3.98×10^{11}J/m^3 results in the full cutting of electrodes with a kerf width span of 23–39 μm. As the cutting speed increases more volume energy is required to cut the electrode, melt current collector, and ablate the active material.

The corresponding measurements for clearance and burr width are shown in Figs. 14 and 15 respectively in terms of cutting speed and volume energy. Clearance of the underside Cu coating was observed in all full cut electrodes where kerf and burr width are also obtained. This characteristic of most multilayer films happens due to thermal and optical properties difference between the active material and current collector materials. The cut edges exhibit clearance width in the range of 27–37 μm. Similarly, to kerf and top width clearance width also decreases as the cutting speed got faster and it increases as the volume energy increases. It is understandable that higher laser power and lower cutting speed lead to the explosion of Cu over larger width to Si active material, due to the low ablation threshold of active material compared to the current collector [35]. The nanosecond threshold volume energy that results in minimum and maximum clearance width is between 3.98×10^{10} -3.98×10^{11} J/m^3.

The burr width of resolidified current collector also decreases as the cutting speed increases and vice versa when the volume energy increases. However, no burr is observed for the no-cut electrodes. Excessive burr mostly occurs when the cutting speed is 500 and 1000 mm/s in the range of 36–51 μm. This is due to high thermal conduction time and high pulse overlap in smaller cutting speeds. For the same cutting speed

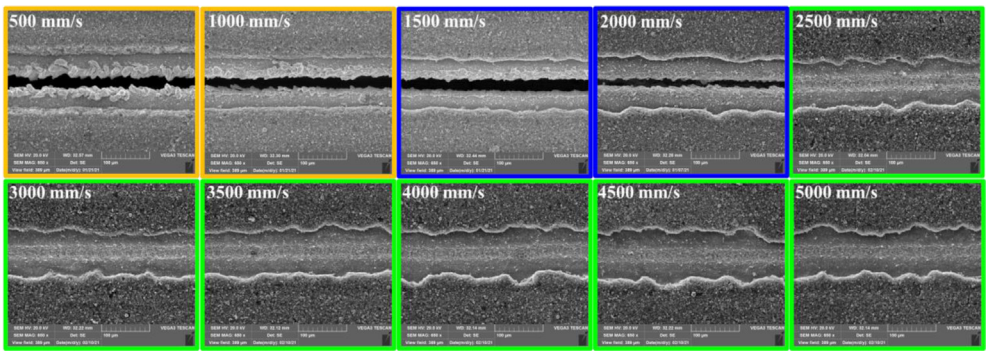


Fig. 7 – SEM image for the laser power of 100 W.

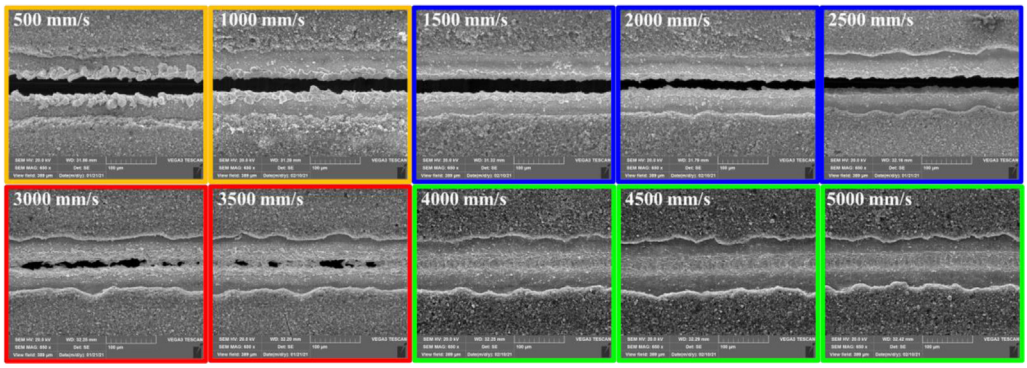


Fig. 8 – SEM image for the laser power of 150 W.

for the corresponding laser powers, the difference in burr width is close. The volume energy that results in kerf width and clearance width also produces burr width.

3.4. *Cutting and energy efficiencies*

For this study, the electrode cutting process consists of mainly the melting of active material and current collector, evaporating of active material, and sublimation of active material. Energy efficiency is the effectiveness of the process in utilizing the laser input energy into the workpiece. Cutting efficiency is a term given to the energy efficiency of full-cut electrodes. In this case, the current collector undergoes melting, and the active material is removed by evaporation, sublimation, and melting. Both cutting and energy efficiency are influenced by process parameters such as laser power, cutting speed, interaction time, and length of cut. These efficiencies were calculated considering the heat transfer efficiency (η_{th}) and processing efficiency (η_p) [23]. The heat transfer efficiency is given by [23]:

$$\eta_{th} = \frac{P_a}{P_i} \tag{3}$$

where, P_a is absorbed laser power by electrode and P_i is laser power input from the source. The processing efficiency is defined as [23].

$$\eta_p = \frac{P_p}{P_a} \tag{4}$$

where, P_p is power used to remove the electrode material by the above-mentioned techniques. Therefore, a combination of these two is used to deliver energy and cutting efficiencies.

$$\eta_c = \eta_p \eta_{th} = \frac{P_p}{P_a}\frac{P_a}{P_i} = \frac{P_p}{P_i} \tag{5}$$

The volumes removed by sublimation, melting, and evaporation are expressed by [23,29].

$$V_{sub_AE} = V_{eva_AE} = V_{melt_AE} = l_g d_{AE} W_{top} \tag{6}$$

$$V_{eva_CC} = V_{melt_CC} = l_g d_{CC} W_{kerf} \tag{7}$$

where, d_{AE} and d_{CC} are the thickness of active material, and current collector respectively, l_g is length covered by laser, $W_{top} and\ W_{kerf}$ are top and kerf width. The energy required to remove the materials is given by.

$$E_{sub} = m_{AE} C_{AE}(T_{sub} - T_O) = \rho_{AE} V_{sub_AE}\{C_{AE}(T_{sub} - T_O)\} \tag{8}$$

$$E_{melt} = m_{AE}\{C_{AE}(T_{melt} - T_O) + L_{melt_AE}\} + m_{CC}\{C_{CC}(T_{melt} - T_O) + L_{melt_CC}\} \tag{9}$$

$$= \rho_{AE} V_{melt_AE}\{C_{AE}(T_{sub} - T_O) + L_{melt_AE}\} + \rho_{CC} V_{melt_CC}\{C_{CC}(T_{melt} - T_O) + L_{melt_CC}\} \tag{10}$$

$$E_{eva} = m_{AE}\{C_{AE}(T_{eva} - T_{melt}) + L_{eva_AE}\} + m_{CC}\{C_{CC}(T_{eva} - T_{melt}) + L_{eva_CC}\} \tag{11}$$

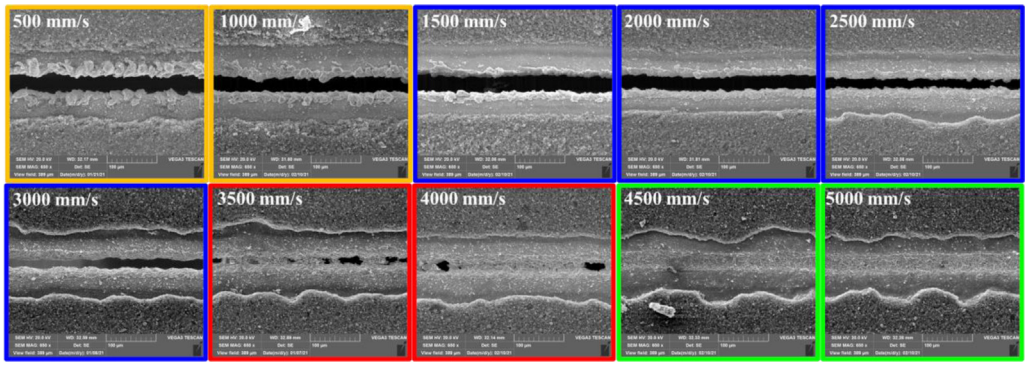


Fig. 9 – SEM image for the laser power of 200 W.

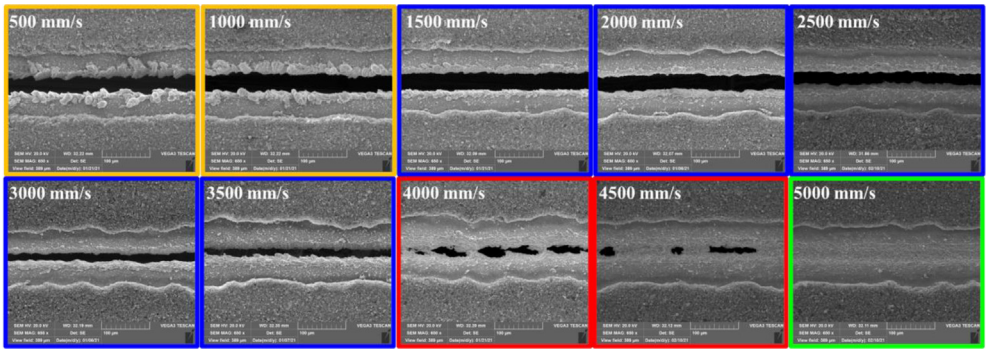


Fig. 10 – SEM image for the laser power of 250 W.

$$= \rho_{AE} V_{eva_AE}\{C_{AE}(T_{eva} - T_{melt}) + L_{eva_AE}\} + \rho_{CC} V_{melt_CC}\{C_{CC}(T_{eva} - T_{melt}) + L_{eva_CC}\} \quad (12)$$

where, m is mass, c is specific heat capacity, ρ is density, T_{sub} is sublimation temprature, T_{melt} is melting temperature, T_{evap} is evaporation temperature, T_o is room temperature, L_{evap} and L_{melt} are latent heat of evaporation and melting. Total energy used to remove the material is given by.

$$E_p = E_{sub} + E_{melt} + E_{evap} \quad (13)$$

Therefore, the laser power used in producing cutting phenomena is calculated as

$$P_p = \frac{E_p}{t_f} \quad (14)$$

$$t_f = \frac{l_g}{v_c} + \frac{D}{v_c} \quad (15)$$

Lee et al. [23,29] have explained the detailed derivation of laser intensity distribution for Gaussian beam, time, laser energy irradiated, and energies required to remove the electrode materials. The energy and cutting efficiency results obtained are indicated in Fig. 16. The energy efficiency ranges between 6.48 and 52.15%. The maximum energy efficiency is achieved at the laser power of 50 W and cutting speed of 3000 mm/s and minimum energy efficiency was calculated at a laser power of 250 W and cutting speed of 500 mm/s The cutting efficiency is also indicated below, it increases as the cutting speed increases and decreases as the laser power decrease. This is due to less interaction time resulting in less thermal conduction. The maximum cutting speed, which produces full cutting leads to high cutting efficiency and productivity. High cutting efficiency of 35% was obtained when using power and cutting speed combinations of 250 W and 3500 mm/s less efficient cutting occurred at the laser power of 250 W and cutting speed of 500 mm/s.

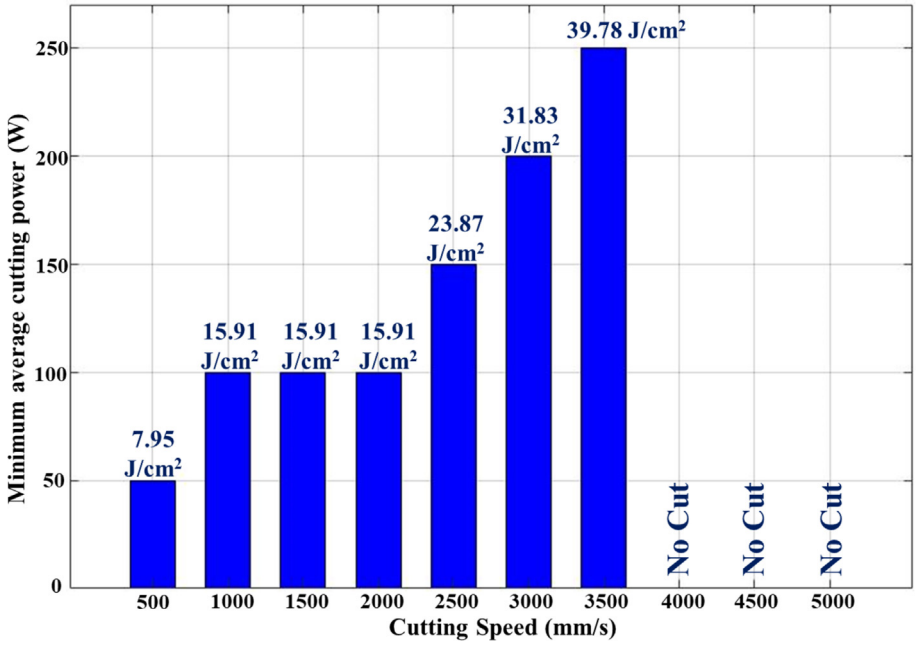


Fig. 11 – Minimum average cutting powers.

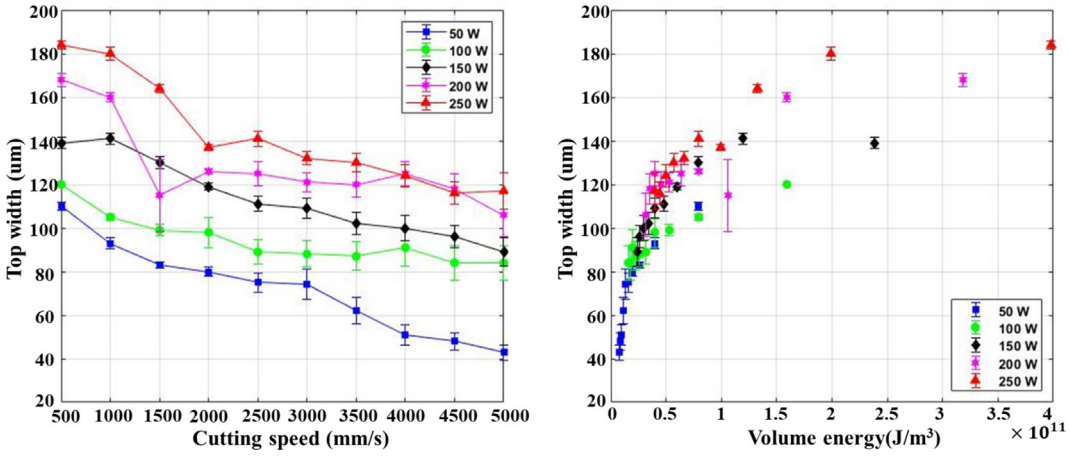


Fig. 12 – Top width versus cutting speed and volume energy.

3.5. *Regression models*

Multiple regression analysis based on response surface methodology (RSM) was used for modeling and predicting the response parameters such as top, kerf, clearance, and burr widths affected by input parameters of laser power and cutting speed by aiming to optimize the response parameters. The general form between dependent and independent variables is unknown therefore, RSM is employed to approximate the responses using a function of input parameters or predictors. The mathematical model can be expressed as the following polynomial function [36–39].

$$y = \beta_0 + \sum_{i=1}^{n} \beta_i X_i + \sum_{i=1}^{n} \beta_{ii} X_i^2 + \sum_{i<j}^{n} \beta_{ij} X_i X_j + \varepsilon \tag{16}$$

where β_0 represents unknown polynomial coefficients estimated by the ordinary least square method, y is the response, X_i and X_j are the independent variables of the i^{th} *and* j^{th} laser process parameters and ε is the error. The models are developed using MATLAB software for top, kerf, clearance, and burr widths as shown below. Where X_1 and X_2 are cutting speed and laser power, respectively.

$$Top\ width = 84.8733 - 0.0214X_1 + 0.5711X_2 + (2.1727 \times 10^{-6})X_1^2 - 6.0857 \times 10^{-4}X_2^2 - (1.3939 \times 10^{-5})X_1X_2 \tag{17}$$

$$Kerf\ width = -1.3746 - 0.0021X_1 + 0.2756X_2 + (8.9466 \times 10^{-8})X_1^2 - (1.4150 \times 10^{-4})X_2^2 - (4.1558 \times 10^{-5})X_1X_2 \tag{18}$$

$$Clearance\ width = 15.091 - 0.0114X_1 + 0.3279X_2 + (1.1001 \times 10^{-6})X_1^2 - (2.3649 \times 10^{-4})X_2^2 - (4.165 \times 10^{-5})X_1X_2 \tag{19}$$

$$Burr\ width = 10.6063 - 0.0095X_1 + 0.2106X_2 + (1.2063 \times 10^{-6})X_1^2 - (2.6939 \times 10^{-4})X_2^2 - (2.3919 \times 10^{-5})X_1X_2 \tag{20}$$

The percentage ability of the prediction models to fit with the experimental model is determined by the determination coefficient (R^2). When the determination coefficient (R^2) is close to 1 implies the mathematical model predicting ability is

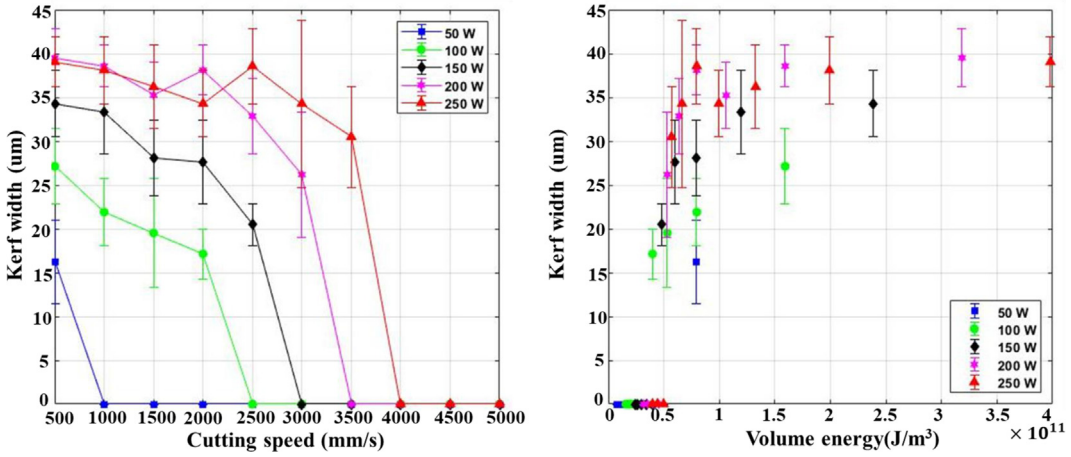


Fig. 13 – Kerf width versus cutting speed and volume energy.

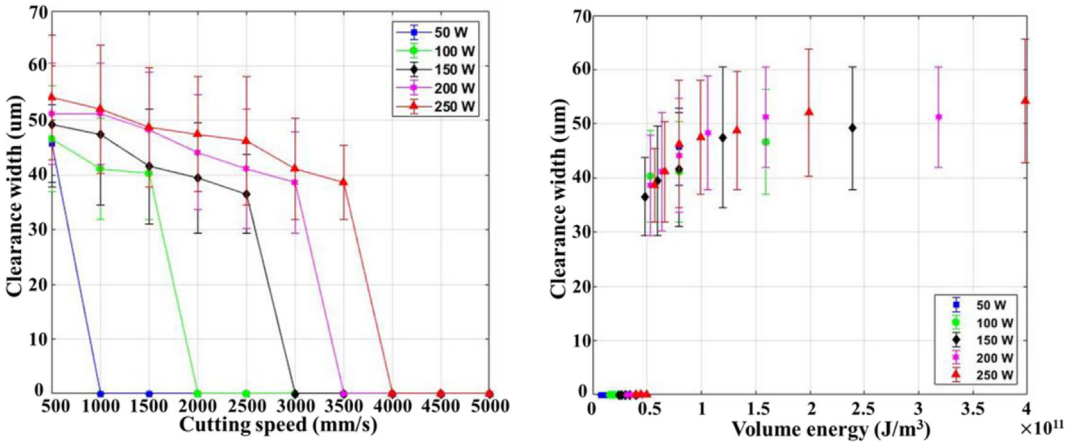


Fig. 14 – Clearance width versus cutting speed and volume energy.

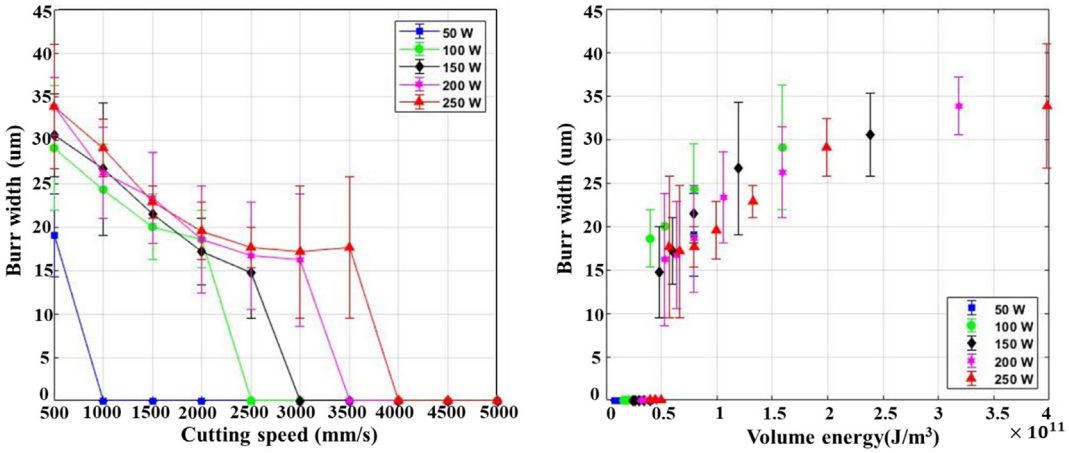


Fig. 15 – Burr width versus cutting speed and volume energy.

good and there is a strong relationship between input parameter and responses. The response surface plots for all cutting widths are shown in Fig. 17.

As shown in Fig. 17, it can be concluded that with the parametric combination where the laser power decreases and cutting speed increases all the cutting widths such as top width, kerf width, clearance width, and burr width decreases. This is because that the accumulated energy is less when the laser power is low and high cutting speed leads to less interaction time producing less heat conduction. For top width, the combination of 250 W laser power and 500 mm/s cutting speed results in maximum top width, and the combination of 50 W and 5000 mm/s produces minimum value. The top width increases rapidly with the increasing laser

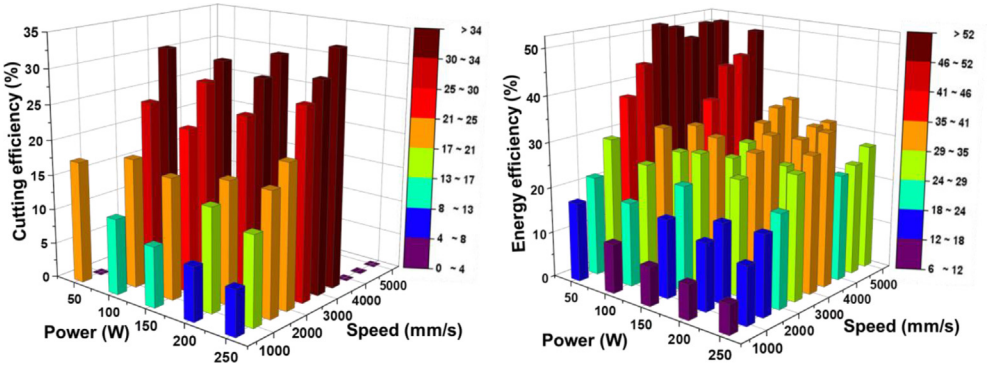


Fig. 16 – Energy and cutting efficiencies.

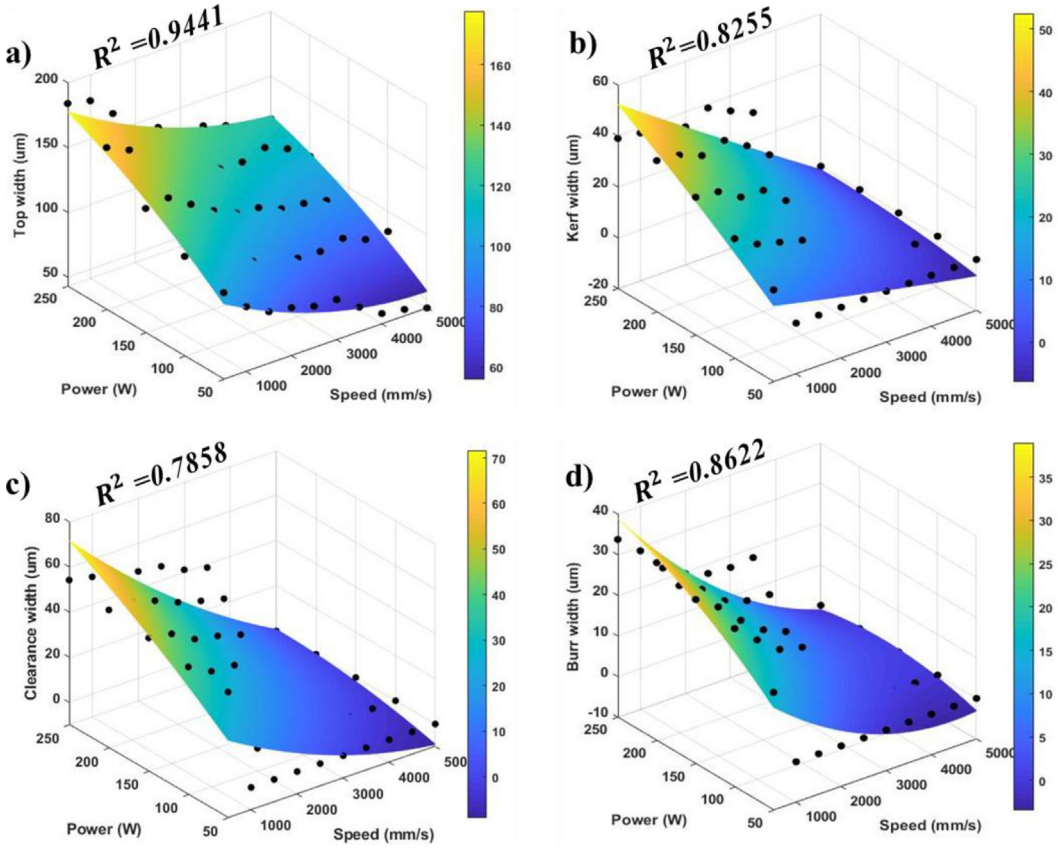


Fig. 17 – Variation of (a) top, (b) kerf, (c) clearance, and (d) burr widths with process parameters.

power. However, the top width increases gradually as the cutting speed increases, and the same trend is observed for kerf, clearance, and burr widths. This can be further explained as high laser power provides more energy deposited on electrode material resulting in mass ablation and low cutting speed increases the pulse overlap and interaction time leading to more ablation and ejection of material. The top width has a determination coefficient of 0.9441, which is close to 1 indicating the developed model has good prediction accuracy. The kerf, clearance, and burr width also have determination coefficients of 0.8255, 0.7858, and 0.8622 consecutively.

RSM-based optimization was used based on the objective to get the optimal combination of parameters yielding the least cutting top, kerf, clearance, and burr widths. The desirability prediction results for optimization of all widths are very close to unity. The optimal parameters obtained by the statistical approach are shown in Table 3 below.

3.6. ANOVA

ANOVA was carried out to study the significant effect and contribution of the input parameters on the quality and characteristics of the responses [40]. The ANOVA results for all cutting widths are presented in Table 4 below. The low P-value and high F-value indicate that there is a strong relationship between laser input parameters and responses. The laser parameters having P-value less than 0.05 are considered as significant parameters to the result. This statical study also proves that all the main effects were significant with all P-values less than 0.005.

It is noticed that the laser power has upper hand over those other parameters in the formation of top width with a percentage contribution of 65.93%, next largest contribution is provided by cutting speed with the contribution of 26.08% and the interaction has a lower contribution of 4.9%, which is considered not to have statical significance. For kerf width, it is realized again that cutting speed is the main influencing factor with a contribution of 53.4%, and the laser power and combined effect follow with percentage contributions of 25.9 and 19.2% respectively. Like kerf width, the clearance width and burr width are greatly or significantly affected by the cutting speed. The clearance width was dependent on the cutting speed by 55.1% and the laser power and combined were significant with contribution levels of 19.89 and 23.25% consecutively. Burr width was mainly influenced by cutting speed with the contribution of 67.72% and the combined and laser power has approximate levels of contribution obtained to be 15.89 and 15.55% respectively.

Table 4 – ANOVA table.

Width	Source	Sum of squares	Mean square	F-value	P-value	Contribution (%)
Top	Power	62,825	15706.3	270.47	<0.0001	65.9317
	Speed	24,852	2761.4	47.55	<0.0001	26.08093
	Power × Speed	4707	130.7	2.25	0.004	4.939762
	Error	2904	58.1			
	Total	95,288				
Kerf	Power	7238.0	1809.50	242.11	<0.0001	25.98885
	Speed	14873.6	1652.62	221.12	<0.0001	53.40534
	Power × Speed	5365.1	149.03	19.94	<0.0001	19.264
	Error	373.7	7.47			
	Total	27850.4				
Clearance	Power	12,749	3187.15	143.3	<0.0001	19.89513
	Speed	35,315	3923.92	176.43	<0.0001	55.10994
	Power × Speed	14,905	414.04	18,362	<0.0001	23.25962
	Error	1112	22.24			
	Total	64,081				
Burr	Power	2362.3	590.58	236.55	<0.0001	15.55414
	Speed	10286.5	1142.94	457.8	<0.0001	67.7296
	Power × Speed	2414	67.06	26.86	<0.0001	15.89455
	Error	124.8	2.5			
	Total	15187.6				

4. Conclusion

In this paper laser cutting phenomena, factors affecting laser cutting efficiency, and quality of lab-made Si anode were studied. This study has led to the following findings:

1. This study uses Si anode in laser cutting research for the first time.
2. The optical properties such as absorptivity, reflectivity, and transmittance of Si anode are measured. The IR laser beam absorptivity and reflectivity were 83.5 and 16.5% respectively.
3. Five types of cutting physical phenomena were observed categorized as (a) excessive full cutting of electrode (b) proper full cutting of electrode (c) partial cutting of electrode (d) partial melting of the current collector and (e) full ablation of active material. They were also defined with their range of volume energy the occurred.
4. Four types of cutting widths such as top width, kerf width, clearance width, and burr width were measured and analyzed in terms of cutting speed, laser power, and volume energy. All the cutting width increases as the cutting speed decreases and laser power increases.
5. Cutting efficiency and energy efficiencies were also discussed. The high cutting speed, which produces full cutting is found to have high cutting efficiency of 32.2%. The highest energy efficiency was obtained at the laser power of 50 W and cutting speed of 3000 mm/s.
6. The mathematical models for top, kerf, clearance, and burr widths are developed using the RSM to show the relation between the input and response parameters. In addition, they are adequate to predict the response parameters.
7. Optimal cutting parameters satisfying the requirement of the industrial standard were identified for all cutting widths. Optimal cutting condition at which the top, kerf, clearance, and burr widths are minimum improves both quality and productivity.
8. The ANOVA results indicate that laser power is more significant than cutting speed and combined effect in influencing the top width with a 65% contribution. However, for the rest three cutting widths kerf, clearance, and burr widths are more affected by cutting speed with the contribution of 53.4, 55.1, and 67.72% respectively.

Declaration of Competing Interest

The authors declare that they have no known competing financial interests or personal relationships that could have appeared to influence the work reported in this paper.

Acknowledgment

The research described herein was sponsored by the National Research Foundation of Korea (NRF) grant funded by the Korean government (MSIP; Ministry of Science, ICT, and Future Planning) (No. 2019R1A2C1089644) and by the KOREA INNOVATION FOUNDATION grant funded by the Korea government (MSIP) (No. 2020-DD-SB-0159).

The opinions expressed in this paper are those of the authors and do not necessarily reflect the views of the sponsors.

REFERENCES

[1] Tarascon JM, Armand M. Issues and challenges facing rechargeable lithium batteries. Materials for sustainable energy: a collection of peer-reviewed research and review articles from. Nature Publishing Group; 2011. p. 171–9.
[2] Kang K, Meng YS, Breger J, Grey CP, Ceder G. Electrodes with high power and high capacity for rechargeable lithium batteries. Science 2006;311(5763):977–80.
[3] Scrosati B, Garche J. Lithium batteries: status, prospects and future. J Power Sources 2010;195(9):2419–30.

[4] Thackeray MM, Wolverton C, Isaacs ED. Electrical energy storage for transportation—approaching the limits of, and going beyond, lithium-ion batteries. Energy Environ Sci 2012;5(7):7854–63.
[5] Lee D, Patwa R, Herfurth H, Mazumder J. Computational and experimental studies of laser cutting of the current collectors for lithium-ion batteries. J Power Sources 2012;210:327–38.
[6] Nitta N, Wu F, Lee JT, Yushin G. Li-ion battery materials: present and future. Mater Today 2015;18(5):252–64.
[7] Suk J, Kim DW, Kang Y. Electrodeposited 3D porous silicon/copper films with excellent stability and high rate performance for lithium-ion batteries. J Mater Chem 2014;2(8):2478–81.
[8] Nitta N, Yushin G. High-capacity anode materials for lithium-ion batteries: choice of elements and structures for active particles. Part Part Syst Char 2014;31(3):317–36.
[9] Liu N, Wu H, McDowell MT, Yao Y, Wang C, Cui Y. A yolk-shell design for stabilized and scalable Li-ion battery alloy anodes. Nano Lett 2012;12(6):3315–21.
[10] Pfleging W. A review of laser electrode processing for development and manufacturing of lithium-ion batteries. Nanophotonics 2018;7(3):549–73.
[11] Etacheri V, Marom R, Elazari R, Salitra G, Aurbach D. Challenges in the development of advanced Li-ion batteries: a review. Energy Environ Sci 2011;4(9):3243–62.
[12] Goodenough JB, Park KS. The Li-ion rechargeable battery: a perspective. J Am Chem Soc 2013;135(4):1167–76.
[13] Lee JK, Oh C, Kim N, Hwang JY, Sun YK. Rational design of silicon-based composites for high-energy storage devices. J Mater Chem 2016;4(15):5366–84.
[14] Megahed S, Ebner W. Lithium-ion battery for electronic applications. J Power Sources 1995;54(1):155–62.
[15] Zhang WJ. A review of the electrochemical performance of alloy anodes for lithium-ion batteries. J Power Sources 2011;196(1):13–24.
[16] Yoshio M, Wang H, Fukuda K, Umeno T, Dimov N, Ogumi Z. Carbon-coated Si as a lithium-ion battery anode material. J Electrochem Soc 2002;149(12):A1598.
[17] Zhang Y, Zhang XG, Zhang HL, Zhao ZG, Li F, Liu C, et al. Composite anode material of silicon/graphite/carbon nanotubes for Li-ion batteries. Electrochim Acta 2006;51(23):4994–5000.
[18] Yim CH, Courtel FM, Abu-Lebdeh Y. A high capacity silicon–graphite composite as anode for lithium-ion batteries using low content amorphous silicon and compatible binders. J Mater Chem 2013;1(28):8234–43.
[19] Liang B, Liu Y, Xu Y. Silicon-based materials as high capacity anodes for next generation lithium ion batteries. J Power Sources 2014;267:469–90.
[20] Wu H, Cui Y. Designing nanostructured Si anodes for high energy lithium ion batteries. Nano Today 2012;7(5):414–29.
[21] Teki R, Datta MK, Krishnan R, Parker TC, Lu TM, Kumta PN, et al. Nanostructured silicon anodes for lithium ion rechargeable batteries. Small 2009;5(20):2236–42.
[22] Herfurth HJ, Patwa R, Pantsar H. Laser cutting of electrodes for advanced batteries. Germany: Proceedings of the LPM; 2010.
[23] Lee D. Investigation of physical phenomena and cutting efficiency for laser cutting on anode for Li-Ion batteries. Appl Sci 2018;8(2):266.
[24] Lee D, Ahn S. Investigation of laser cutting width of LiCoO2 coated aluminum for lithium-ion batteries. Appl Sci 2017;7(9):914.
[25] Demir AG, Previtali B. Remote cutting of Li-ion battery electrodes with infrared and green ns-pulsed fibre lasers. Int J Adv Manuf Technol 2014;75(9–12):1557–68.
[26] Lee D. Modeling of high speed remote laser cutting of electrodes for lithium-ion batteries (Doctoral dissertation). 2012.
[27] Lee D, Patwa R, Herfurth H, Mazumder J. Parameter optimization for high speed remote laser cutting of electrodes for lithium-ion batteries. J Laser Appl 2016;28(2):22006.
[28] Lee D, Suk J. Laser cutting characteristics on uncompressed anode for lithium-ion batteries. Energies 2020;13(10):2630.
[29] Lee D, Oh B, Suk J. The effect of compactness on laser cutting of cathode for Lithium-Ion Batteries using continuous fiber laser. Appl Sci 2019;9(1):205.
[30] Luetke M, Franke V, Techel A, Himmer T, Klotzbach U, Wetzig A, et al. A comparative study on cutting electrodes for batteries with lasers. Physics Procedia 2011;12:286–91.
[31] Lutey AH, Fortunato A, Ascari A, Carmignato S, Leone C. Laser cutting of lithium iron phosphate battery electrodes: characterization of process efficiency and quality, vol. 65. Optics & Laser Technology; 2015. p. 164–74.
[32] Pfleging W, Gotcu P, Smyrek P, Zheng Y, Lee JK, Seifert HJ. Lithium-ion battery—3D micro-/nano-structuring, modification and characterization. In: Laser micro-nano-manufacturing and 3D microprinting. Cham: Springer; 2020. p. 313–47.
[33] 박주영. Laser Cutting of cathode electrode (LiFePO4) of Li-ion battery (doctoral dissertation, 서울대학교 대학원). 2019.
[34] Lee D, Mazumder J. Effects of laser beam spatial distribution on laser-material interaction. J Laser Appl 2016;28(3):32003.
[35] Lutey AH, Fortunato A, Carmignato S, Fiorini M. High speed pulsed laser cutting of LiCoO2 Li-ion battery electrodes, vol. 94. Optics & Laser Technology; 2017. p. 90–6.
[36] Xing Y, Liu L, Hao X, Wu Z, Huang P, Wang X. Micro-channels machining on polycrystalline diamond by nanosecond laser, vol. 108. Optics & Laser Technology; 2018. p. 333–45.
[37] Gadallah MH, Abdu HM. Modeling and optimization of laser cutting operations. Manuf Rev 2015;2:20.
[38] Chatterjee S, Mahapatra SS, Abhishek K. Simulation and optimization of machining parameters in drilling of titanium alloys. Simulat Model Pract Theor 2016;62:31–48.
[39] Chatterjee S, Mahapatra SS, Bharadwaj V, Upadhyay BN, Bindra KS. Prediction of quality characteristics of laser drilled holes using artificial intelligence techniques. Eng Comput 2021;37(2):1181–204.
[40] Chatterjee S, Mahapatra SS, Bharadwaj V, Choubey A, Upadhyay BN, Bindra KS. Drilling of micro-holes on titanium alloy using pulsed Nd: YAG laser: parametric appraisal and prediction of performance characteristics. Proc IME B J Eng Manufact 2019;233(8):1872–89.